# SANDIA REPORT

SAND97-0580 • UC-706
Unlimited Release
Printed March 1997



# Optical Waveguide Tamper Sensor Technology

Richard F. Carson, Michael A. Butler, Michael B. Sinclair, Stephen A. Casalnuovo, Arnold J. Howard, John P. Hohimer, Michael L. Lovejoy

Prepared by
Sandia National Laboratories
Albuquerque, New Mexico 87185 and Livermore, California 94550

Sandia is a multiprogram laboratory operated by Sandia Corporation, a Lockheed Martin Company, for the United States Department of Energy under Contract DE-AC04-94AL85000.



Sandia National Laboratories

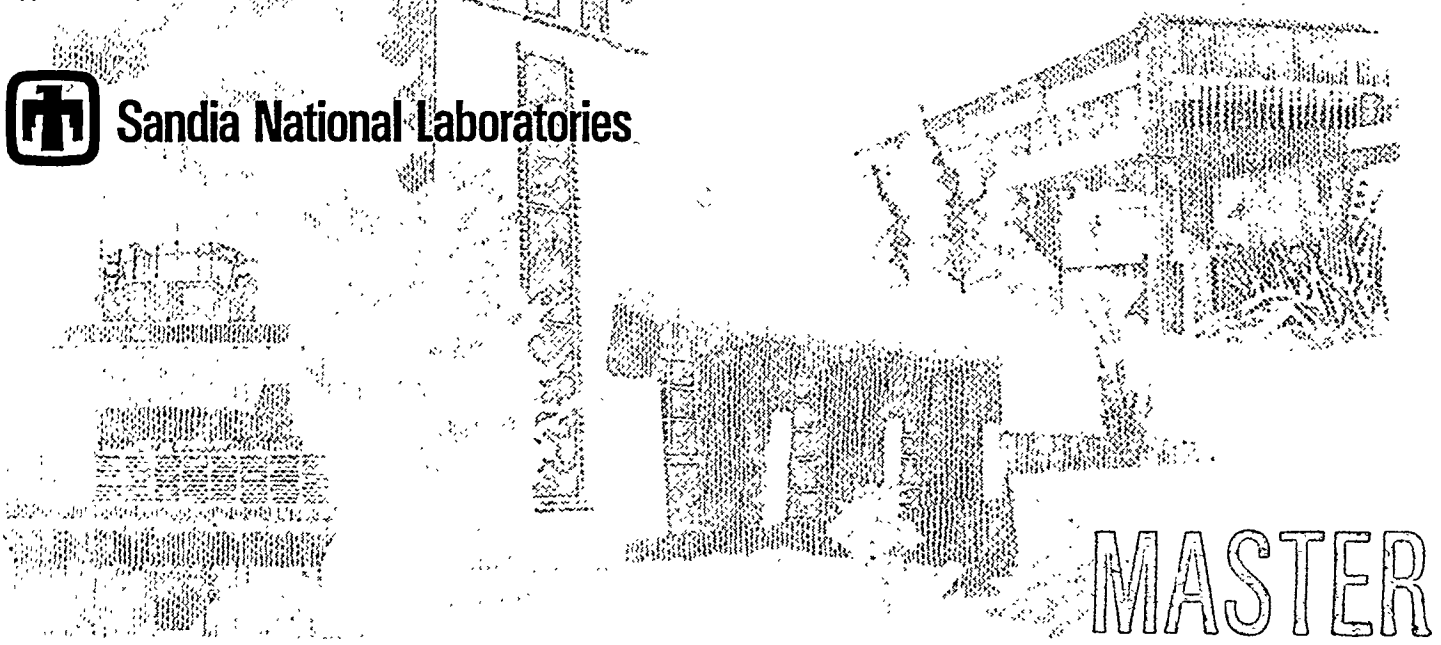

Issued by Sandia National Laboratories, operated for the United States Department of Energy by Sandia Corporation.


Available to DOE and DOE contractors from
Office of Scientific and Technical Information
P.O. Box 62
Oak Ridge, TN 37831

Prices available from (615) 576-8401, FTS 626-8401

Available to the public from
National Technical Information Service
U.S. Department of Commerce
5285 Port Royal Rd
Springfield, VA 22161

NTIS price codes
Printed copy: A03
Microfiche copy: A01

SAND97-0580
Unlimited Release
Printed March 1997

Distribution
Category UC-706

# Optical Waveguide Tamper Sensor Technology

Richard. F. Carson, Michael A. Butler, Michael B. Sinclair,
Stephen A. Casalnuovo, Arnold J. Howard, John P. Hohimer, and Michael L. Lovejoy

Advanced Devices & Applications Department
Sandia National Laboratories
P.O. Box 5800, Albuquerque, NM 87185-5800

## Abstract

Dielectric optical waveguides exhibit properties that are well suited to sensor applications. They have low refractive index and are transparent to a wide range of wavelengths. They can react with the surrounding environment in a variety of controllable ways. In certain sensor applications, it is advantageous to integrate the dielectric waveguide on a semiconductor substrate with active devices. In this work, we demonstrate a tamper sensor based on dielectric waveguides that connect epitaxial GaAs-GaAlAs sources and detectors. The tamper sensing function is realized by attaching particles of absorbing material with high refractive index to the surface of the waveguides. These absorbers are then attached to a lid or cover, as in an integrated circuit package or multi-chip module. The absorbers attenuate the light in the waveguides as a function of absorber interaction. In the tamper indicating mode, the absorbers are placed randomly on the waveguides, to form a unique attenuation pattern that is registered by the relative signal levels on the photodetectors. When the lid is moved, the pattern of absorbers changes, altering the photodetector signals. This dielectric waveguide arrangement is applicable to a variety of sensor functions, and specifically can be fabricated as a chemical sensor by the application of cladding layers that change their refractive index and/or optical absorption properties upon exposure to slected chemical species. An example is found in palladium claddings that are sensitive to hydrogen. A description of designs and a basic demonstration of the tamper sensing and chemical sensing functions is described herein.

## Acknowledgments

This work was supported by the United States Department of Energy under Contract DE-AC04-94AL85000. Sandia is a multiprogram laboratory operated by Sandia Corporation, a Lockheed Martin Company, for the United States Department of Energy. This project was performed under Sandia's Laboratory-Directed Research and Development (LDRD) program.

The authors wish to thank D. Webb, R. Shul, and G. A. Vawter for processing support and process development, respectively. The authors would also like to thank R. P. Schneider and J.J. Figiel for the OMVPE grown tamper sensor diode structures. We would also like to thank J. Zolper for the proton isolation implant which was performed on one of the tamper sensor wafers.

# Contents

## Figures



## Tables

# Optical Waveguide Tamper Sensor Technology

## 1. INTRODUCTION

Dielectric waveguides have been demonstrated for a number of integrated optics applications, including passive (glass) and active ($LiNbO_3$) devices [1],[2]. Because they are transparent to a wide range of wavelengths and can be made low loss, dielectric waveguides have been proposed and realized in organic material systems such as polyimide for use in general optical interconnect work [3]. In support of these applications, dielectric waveguides have also been constructed using glass structures integrated on the surfaces of GaAs and silicon wafers [4],[5]. Because they have a relatively low refractive index, dielectric optical waveguides have also been shown to exhibit unique properties when brought in contact with a thin layer of absorbing material having a higher refractive index than the guide [6]. These properties have been used to create sensors that measure optical constants and layer thickness in absorbing materials[7],[8]. Thus, the properties can be closely related to the optical testing function. In this work, we integrate dielectric waveguides with active GaAs devices and expand on the sensor functions that can be realized in this waveguide material system.

### 1.1 Tamper Sensor Concept

The basic concept for a tamper sensor is illustrated in Figure 1, which shows an operational schematic of the device cross-section. The forward-biased LED (with injected current $I_f$) emits light, which travels along the waveguide. When it encounters an absorber, a portion of the light is coupled out. That light which reaches the unbiased detector produces an open-circuit electrical voltage ($V_{oc}$). Photocurrent can also be detected when the photodiode is under a reverse bias. The amount of light reaching the detector is dependent on the size and shape of the absorber. Absorbers are randomly distributed along the surface of the waveguide, as shown. The combination of absorbers encountered in a waveguide path then

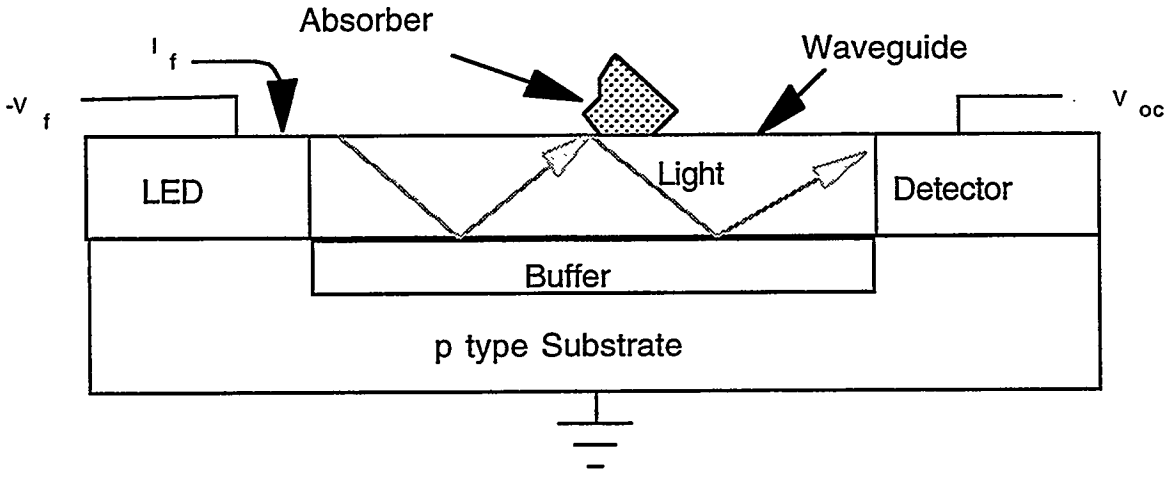


**Figure 1** Operational schematic showing LED, detector, waveguide, and absorber.

produces a given signal at the photodetector. These absorbers are attached to a lid as on an IC package or Multi-Chip Module (MCM). When the lid is moved, the pattern of absorbers changes, altering the photodetector signals. Here, polymer or dielectric waveguides are used, since they are most sensitive to changes induced by high refractive index absorbers such as silicon or metal particles.

The function of the diode structure is determined by magnitude and polarity of the applied bias. In forward bias it can be an emitter, as shown in Figure 1. With reverse or zero bias it functions as a detector. The transfer function between the emitter and detector is determined by coupling efficiency to and from the waveguide, quantum efficiency of the emitter and detector, and the loss along the waveguide. Disturbances of the absorbing elements on the waveguide will then change the transfer function. It is this change in transfer function that constitutes the tamper sensing. As will be described, the absorbers may also be sensitive to chemicals, thus enabling a chemical sensor function using the same waveguide structure and change in transfer function.

## 1.2 Tamper-Sensing Arrays

The waveguide sensing devices can be constructed in an array pattern as in Figure 2 such that differential changes between various photodetectors exclude normal environmental effects from erroneous detection. In particular, the proposed array of waveguide "spokes" around a central LED device could make use of the omni-directional output of the LED. In this arrangement, the power would be applied through the designated contact pad, and the signals from each detector would appear on its respective contact pad. A common, conductive semiconductor substrate would be used, as in Figure 1. Since ratios of signals at the photodetectors are detected, any overall variations in the overall LED output would be excluded from

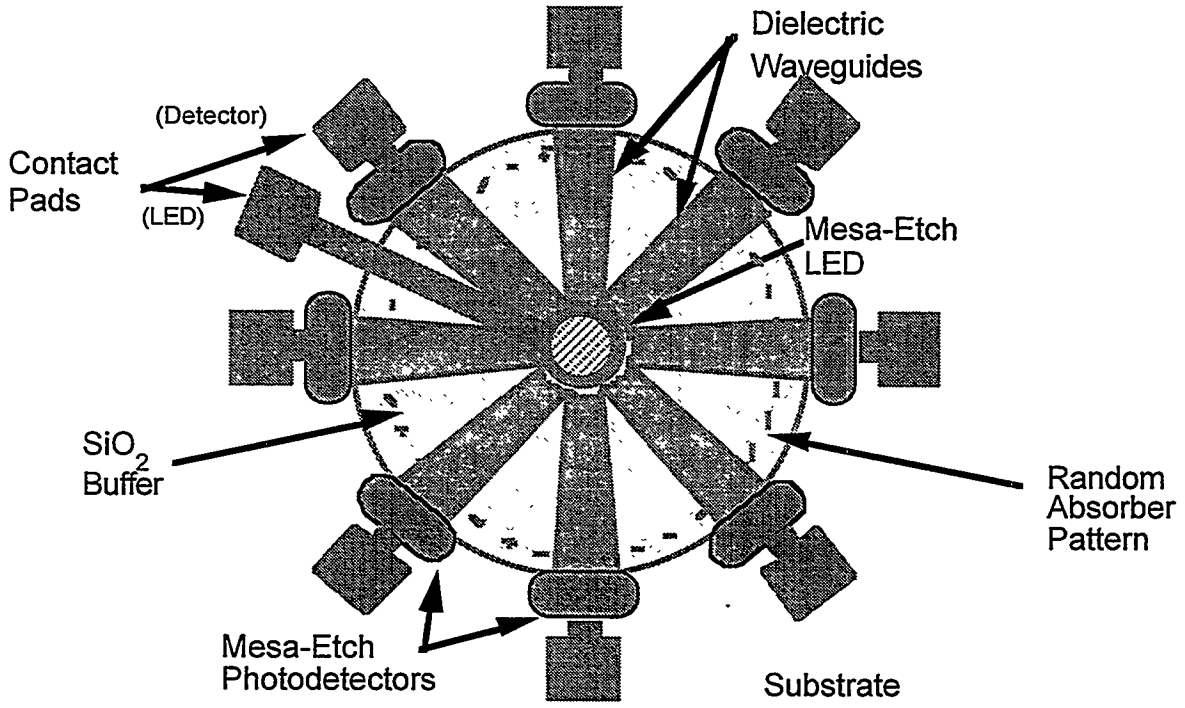


**Figure 2** Multiple waveguides and detectors with a single LED. Ratios of signals are sensed at the detectors.

the sensor function. The array of absorbers can be placed randomly on the waveguides so as to form a non-reproducible pattern, that would be disturbed during a tamper event. Alternately, a chemical sensor array can be realized by the application of various chemically-sensitive absorbers in place of the random tamper-sensing absorber region of Figure 2. In either case, the basic transfer function described in Figure 1 would be realized and modified (according to state of tamper or chemical exposure) for each spoke of the wheel. It is the enabling characteristic of the tranfer function and its sensitivity to tampering or chemicals that will be demonstrated within the scope of this report.

## 1.3 Chemical Sensing

Other sensor functions besides tamper sensing can also be realized. Specifically, the device can be configured as a chemical sensor. This is easily done by the application of a chemically sensitive cladding layer on the waveguides in place of the absorber in Figure 1. This chemical sensor could be used in a variety of operating modes. When inserted into an IC or MCM package, the chemical sensor could detect a chemical attack on the package, thus extending the modes of use in a tamper sensing environment. This device could also be configured specifically as a chemical sensor as in the package arrangement of Figure 3. Here, the device is packaged so as to expose a chemically sensitive cladding layer to the external environment. When certain chemicals are present, the cladding absorption and refractive index are changed, changing the attenuation along the waveguide path and thus changing the signal at the detector. The absorber is allowed to interact with an external stimulus (such as a chemical species) that would change its refractive index and/or absorption. Non-absorbing cladding layers have been proposed on optical waveguide sensors to increase evanescent field interaction with external chemical species [9]. Here, the sensitivity of the interaction could be tailored by choosing an absorbing layer thickness to tune in a resonance point of guided-wave interaction. As stated, these changes have been used to measure optical properties [7],[8]. If those properties change as a result of chemical interaction, then the chemical can be detected. Thus, this optical waveguide technology has the potential to produce a chemical sensor. The versatility of such a chemical sensor could be extended by the use of an array, as in Figure 2, where the random pattern of absorbers is replaced by an array of different chemical sensing claddings.

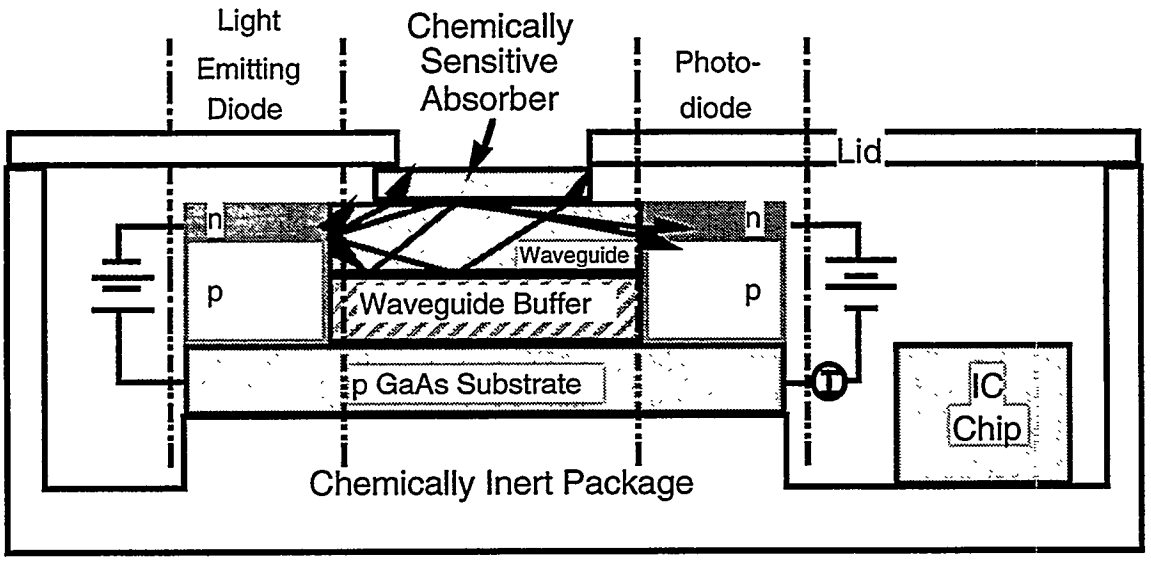


**Figure 3** Operation as a chemical sensor. The waveguide is packaged to allow the chemically-sensitive absorber to encounter the chemical species under test.

## 1.4 Design, Fabrication, and Testing

The design process starts with guided-wave calculations for the active device and waveguide. These calculations are described here in terms of basic design parameters and tolerance for the guided-wave structures of the active diode and passive waveguide devices. The guided-wave calculations for a palladium-clad chemical sensor are also presented. Next, device and waveguide processing and fabrication is discussed. This is followed by electrical and optical performance of the diode devices including forward bias (LED) parameters and reverse bias detector parameters. An improved Graded Index Separate Confinement Heterostructure (GRINSH) device cross-section is also introduced. Waveguide measurements and the results of tests on the combined device will then be reviewed. Absorber interaction experiments are also described and hydrogen sensor functional results are discussed.

## 2. OPTICAL STRUCTURE

Figure 4 shows an optical cross-section of the diode-waveguide interface. The heterojunction epitaxial layers are grown on the GaAs wafer as in the figure. The structure contains GaAs as an emitting and absorbing layer, with a refractive index of 3.5 as shown. The $Al_{.3}$ $Ga_{.7}$ As and $Al_{.4}$ $Ga_{.6}$ As layers act as low-absorption waveguide buffer layers, since their refractive indices (3.4 and 3.33) are lower than the GaAs layer. These areas are mesa-etched to form the LED and photodiode devices. The refractive index and thickness of the dielectric or polymer guide and $SiO_2$ buffer layers are chosen so that the field distributions of the optical waves are closely matched as in Figure 4. These design parameters have been modeled and optimized by the use of one-dimensional guided-wave calculations, using a code called MODEIG [10]. Note in Figure 4 that the modes must match very closely in shape and peak point in order to achieve good coupling efficiency between the dielectric waveguide and the active GaAs-GaAlAs device. This will call for approximately 0.1 to 0.2 μm accuracy in layer thicknesses and etch depths during the construction of the tamper sensor. Such tolerances are readily obtainable with modern semiconductor device processing techniques.

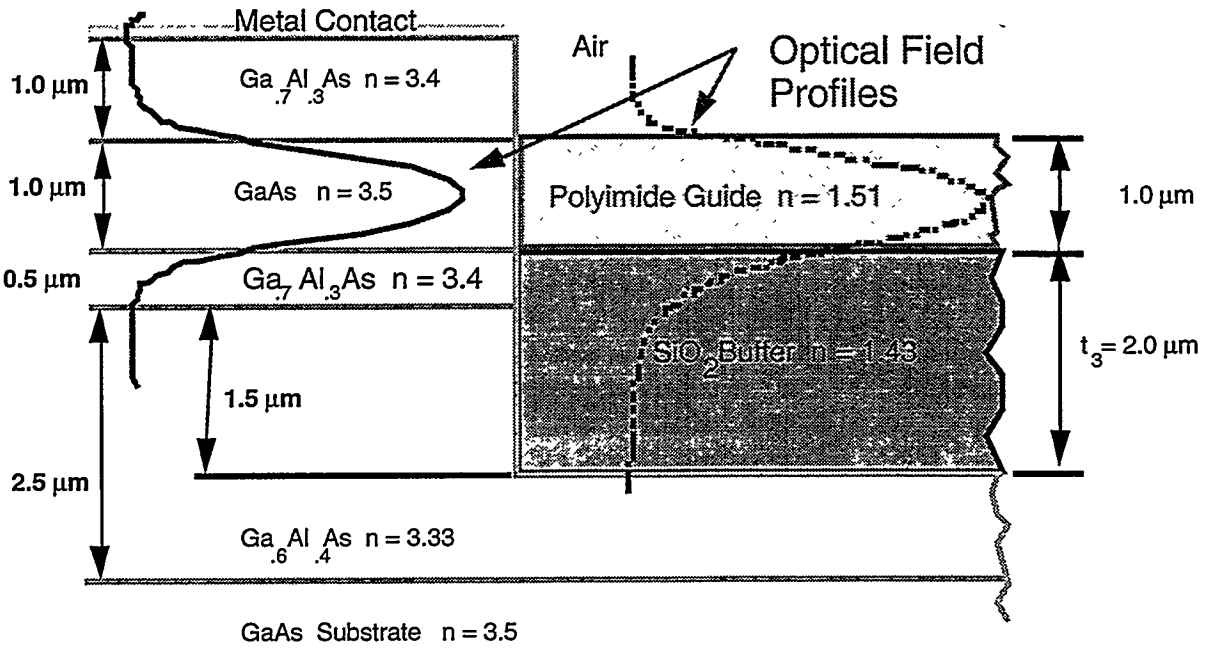


**Figure 4** Optical cross-section of the active device and waveguide combination showing various layers and their refractive indices.

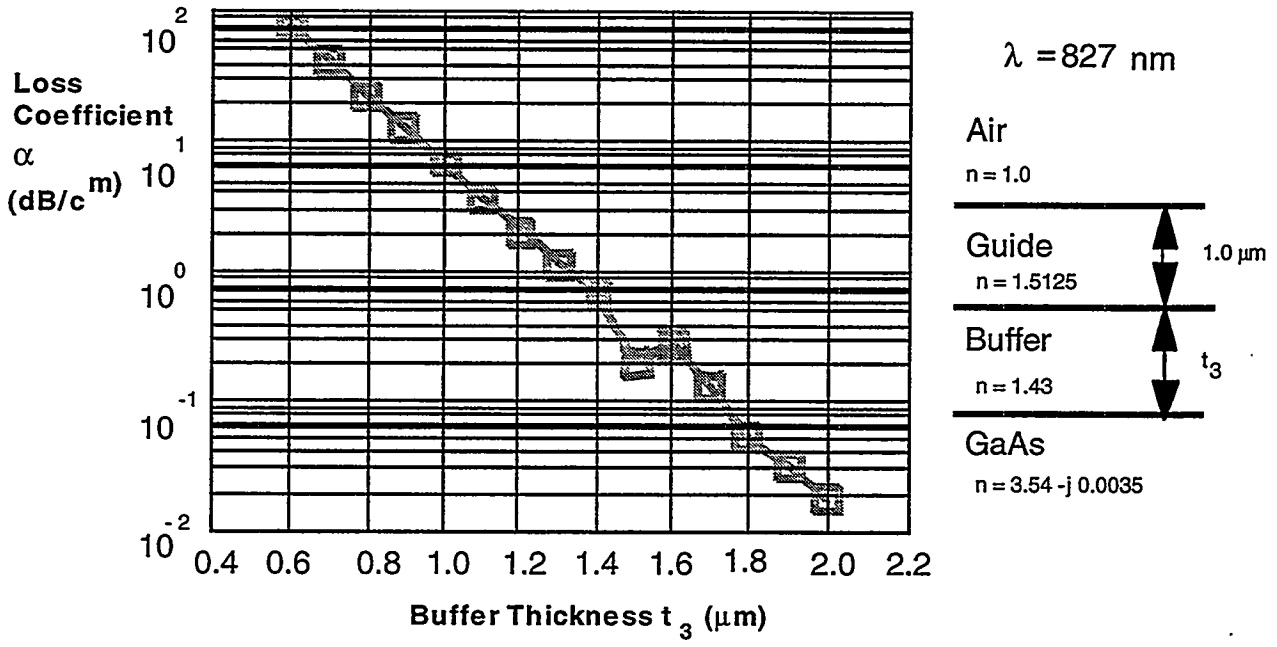


**Figure 5** Waveguide attenuation for the fundamental waveguide mode as a function of buffer layer thickness $t_3$ in the structure shown.

## 2.1 Dielectric Waveguide Optimization

Our calculations have led to the design of Figure 4, which maximizes the coupling of the waveguides to and from the GaAs devices for the lowest order waveguide mode. To keep light losses low, the $SiO_2$ buffer must be thick enough so that the field distributions of the light do not significantly couple into the high-absorption GaAs substrate. This constraint sets the etch and deposition parameters that will be needed for device fabrication. We have thus calculated losses as a function of waveguide buffer layer thickness as in Figure 5 with the waveguide structure shown in the inset. Here, the waveguide buffer layer is varied while the waveguide thickness and the refractive indices of the entire structure are held constant. Note that the waveguide attenuation rises exponentially as buffer layer thickness is reduced, and is especially high below about 1 μm. We have thus chosen a buffer layer thickness of 2.0 μm, as in Figure 4, which should keep losses below 0.02 dB/cm at 827 nm. For the experimentally determined 860 nm output wavelength of the LED, these losses would be slightly higher.

As part of the design process for the dielectric waveguide, the field profiles for the two possible mode orders in the dielectric guide structure were also calculated. These profiles appear in Figure 6. Note for the 0th order (fundamental) mode that the evanescent field tail does not extend significantly into the semiconductor substrate. For the first order mode, there is significant interaction with the underlying layer of $Ga_{0.6}$ $Al_{0.4}$ As. This indicates that, while the waveguide will support two mode orders, the higher order guided wave mode will be attenuated as it propagates down the guide due to coupling into the substrate. Thus, in order to create an optimal structure for integration with the GaAs, the waveguide refractive index must be high, with respect to the buffer layer. Also, both the waveguide thickness and that of the buffer layer must be large enough so that the 0th order evanescent field tail does not interact

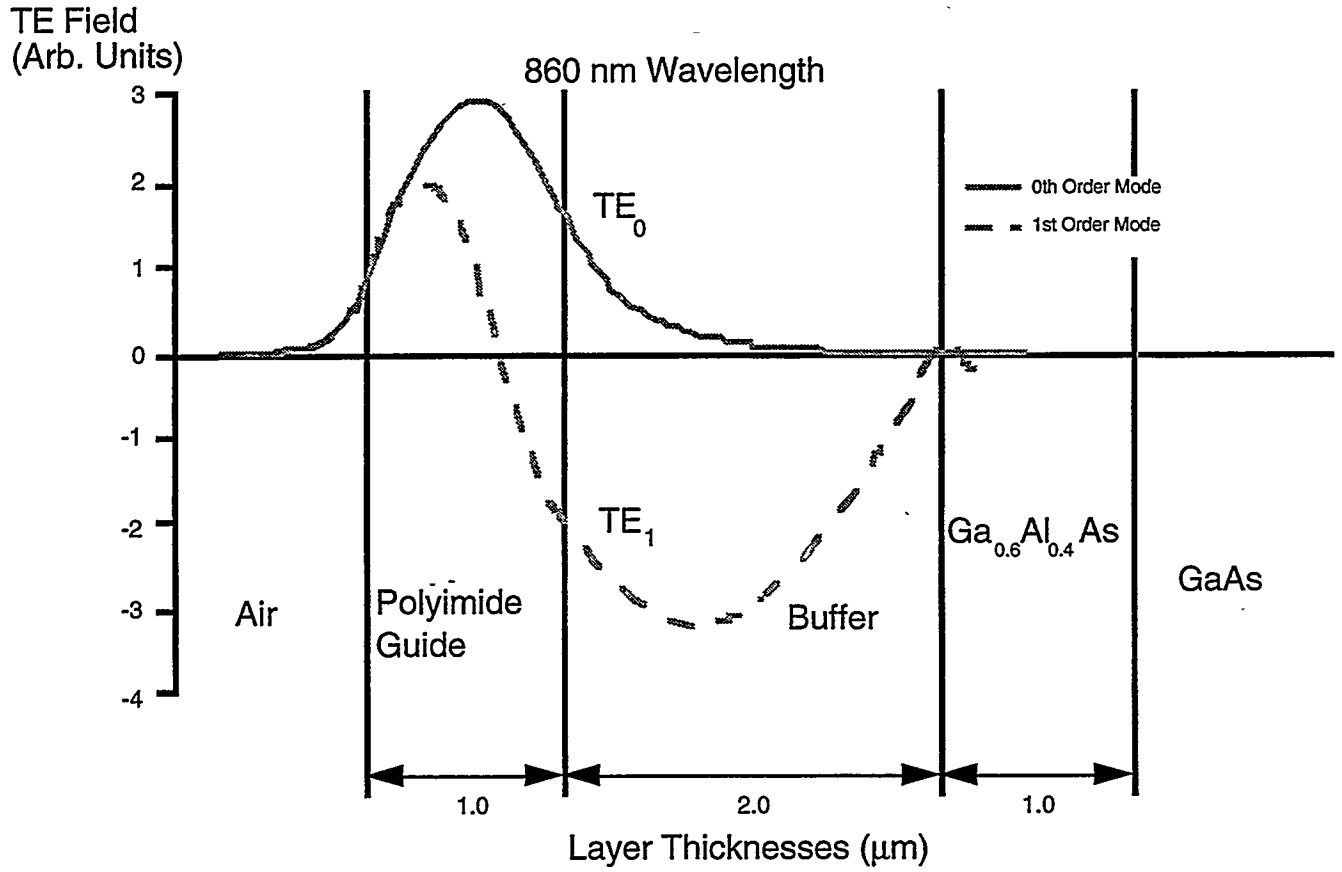


**Figure 6** Field strengths of the $TE_0$ and $TE_1$ waveguide modes.

with the underlying semiconductor. This implies that the waveguide will actually support more than one mode. Further optimization for the chemical sensing function is discussed in Section 2.2.

## 2.2 A Pd-Clad Waveguide Structure for $H_2$ Sensing

As indicated in Figure 3, the integrated waveguide sensor structure can be constructed so as to perform chemical sensing functions. This sensor is based on the fact that a thin layer of Pd will change its optical absorption and refractive index when exposed to hydrogen ($H_2$) gas. This effect has been used to construct optical fiber probes for remote gas sensing [11].

The MODEIG program was used to calculate guided-wave profiles and parameters for the Pd-clad waveguide structure shown in the inset of Figure 7. Here, the refractive indices of the guide and buffer layers were chosen to match measured values from laboratory experiments. The guide thickness also matched experimental values. For ease of calculation, the structure was approximated with a semi-infinite buffer layer. This approximation is valid because of the small evanescent field leakage into the substrate, as described above. Because the Pd film is optically lossy, it is characterized by a complex refractive index. The index values with and without exposure to a 10% $H_2$ atmosphere were assumed to

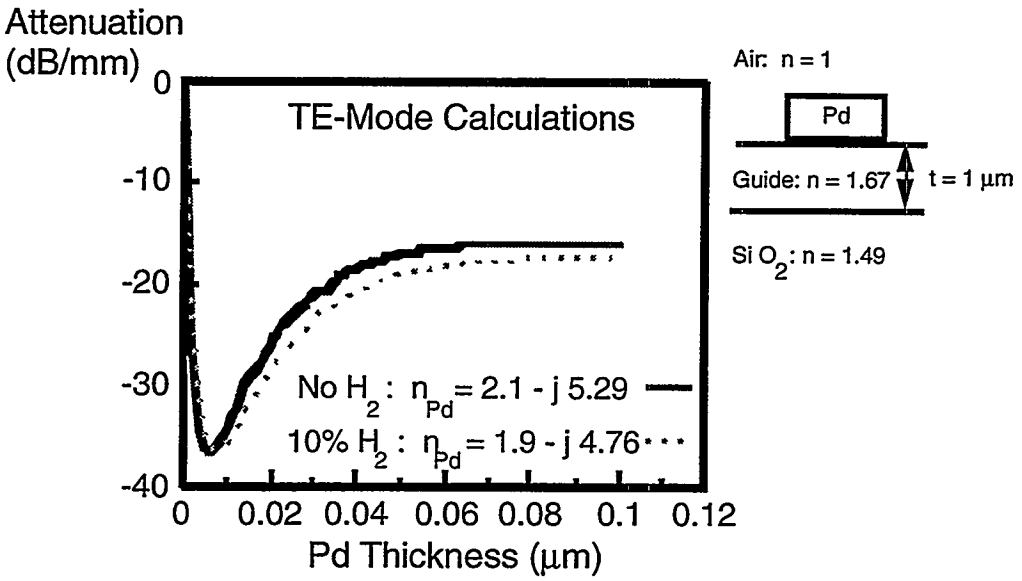


**Figure 7** Calculated losses for a Pd-clad waveguide with and without $H_2$ exposure. Wavelength is 860 nm.

change as indicated on the graph, and the attenuation coefficient for the four-layer lossy waveguide was calculated. It is shown with a negative sign in this graph to indicate that it is a loss coefficient.

Note in Figure 7 that the Pd shows an attenuation maximum just below a 10 nm thickness. Note also that below that critical thickness, the slope of the attenuation vs. thickness curve is very steep and that relatively large attenuation changes with hydrogen exposure can occur.

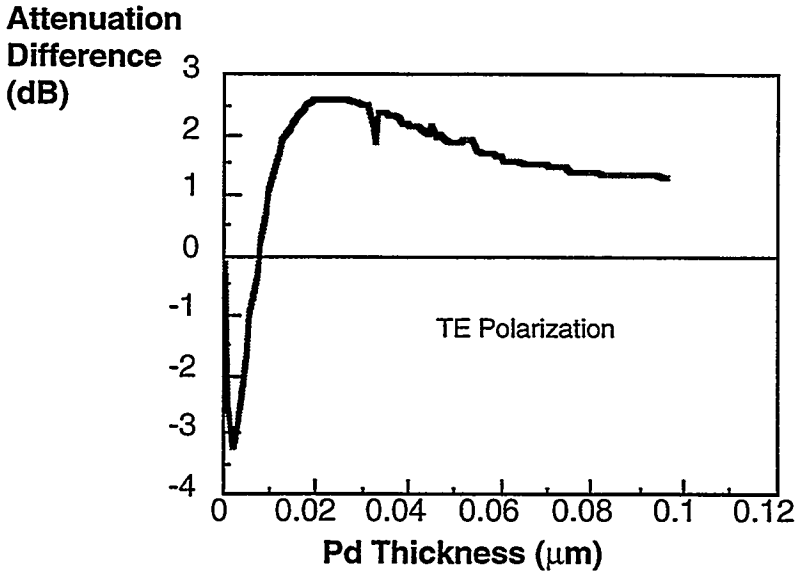


**Figure 8** Calculated attenuation difference with and without $H_2$ for a 1 mm long Pd cladding on a dielectric waveguide for a wavelength of 860 nm.

The attenuation difference without and with the 10% $H_2$ atmosphere is plotted in Figure 8 for a 1 mm length of Pd cladding on the indicated waveguide. Note that for a 2 nm Pd thickness, there is a maximum of $H_2$ sensitivity based on an attenuation difference of about 3.0 dB. The overall calculated waveguide attenuation is about 25 dB, so a large initial signal would be needed to assure a reasonable dynamic range. Near the maximum attenuation at 7 nm, the sign of the difference changes and at larger thickness values there is greater attenuation with hydrogen present than without. At these larger Pd thickness values, there is about 1.5 dB more attenuation when the hydrogen is present

For the TM polarization in this waveguide, the calculated losses were huge, on the order of 300 dB per mm. This is expected, since the TM-polarized light tends to form high-loss surface plasma modes in a metal-clad waveguide structure. In fact, metal claddings are often used as TM mode suppression filters on planar dielectric waveguides [12].

Variations on the waveguide structure were modeled in an attempt to maximize the chemical sensing function while minimizing the total loss in the clad-waveguide structure. A five-layer version of the guide in Figure 7 was modeled, using a thin $SiO_2$ buffer layer in between the cladding and the guide. This type of buffer layer has been shown to reduce attenuation in metal-clad waveguides. In this case the attenuation was reduced by 60 percent for an $SiO_2$ layer thickness of 0.1 μm, but the maximum difference between the 10 percent $H_2$ and non-$H_2$ conditions scaled down accordingly.

Several other waveguide variations were also tried in order to understand the effect of guide structure on overall attenuation and Hydrogen sensing capability. Low overall optical loss had previously been reported in a $LiNbO_3$ version of a Pd-Clad waveguide hydrogen sensor [13]. Here, the attenuation was so low that a Mach-Zehnder interferometer was required to detect the hydrogen. We modeled this structure as a planar waveguide and likewise obtained low attenuation as in Figure 9. In order to separate out the effect of waveguide structure from that of overall refractive index, we further modeled a "D-Fiber" type of slab waveguide. Here, the planar layers approximated the thick, low waveguide

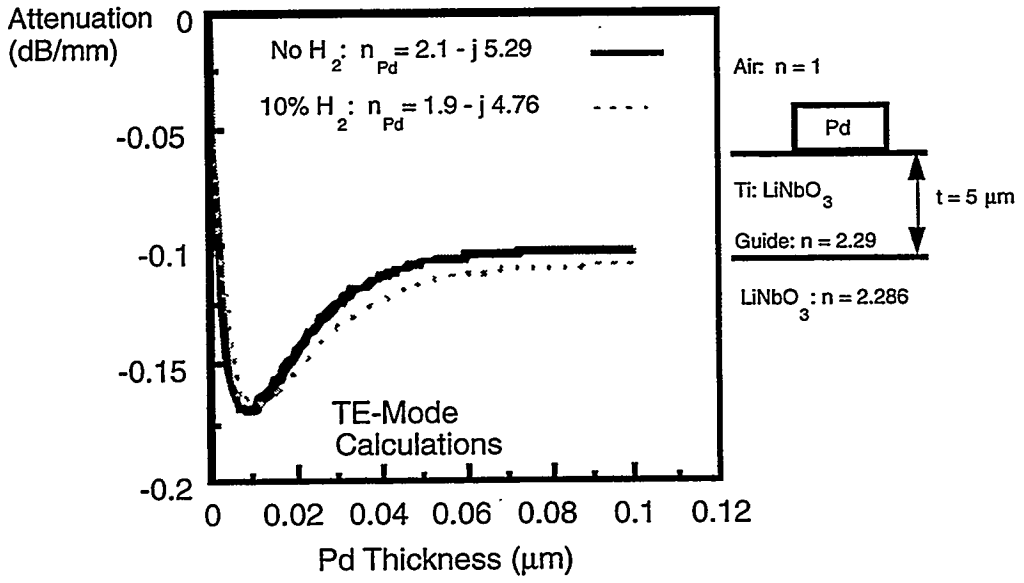


**Figure 9** Attenuation of a Pd-clad $LiNbO_3$ waveguide with and without exposure to 10 percent $H_2$. Wavelength is 860 nm.

structure of a "D-shaped" single mode optical fiber. Though refractive index was lower than that of the $LiNbO_3$ waveguide, both represent a structure where the refractive index difference between the core and the buffer is very low (a "low $\Delta n$" type of waveguide structure. Both the $LiNbO_3$ and the slab fiber guide structures showed very low overall attenuation (and a corresponding low hydrogen sensing capability). This was due to very weak interaction with the cladding on the top surface. For that reason, these structures would not be suitable as Pd-clad $H_2$ sensor waveguides, unless used in an interferometer structure. In addition, the evanescent field tails on these low $\Delta n$ guides extend deep into the buffer, (which accounts for their weak cladding interaction), Thus, they would be impractical for use with the basic guide structure of Figure 1 because of the thickness of buffer needed to prevent unwanted interaction with the semiconductor substrate. These low $\Delta n$ structures do, however, give us insight as to how the dielectric waveguide structure influences the overall sensitivity of the Pd-clad waveguide.

In order to maximize hydrogen sensitivity, a thin, high $\Delta n$ structure such as a $Si_3N_4$ guide on a $SiO_2$ buffer could be used, as in Figure 10. For this structure, the evanescent field tail into the buffer would short, and there is a large interaction with the Pd metal. Because of the resulting large attenuation, (up to several hundred dB per mm, as shown), a very large initial signal would be required or a short length of Pd would be placed on the waveguide. A compromise Pd-clad waveguide structure such as that of Figure 4 would then appear to be the best choice for a hydrogen sensor because the attenuation is more controllable.

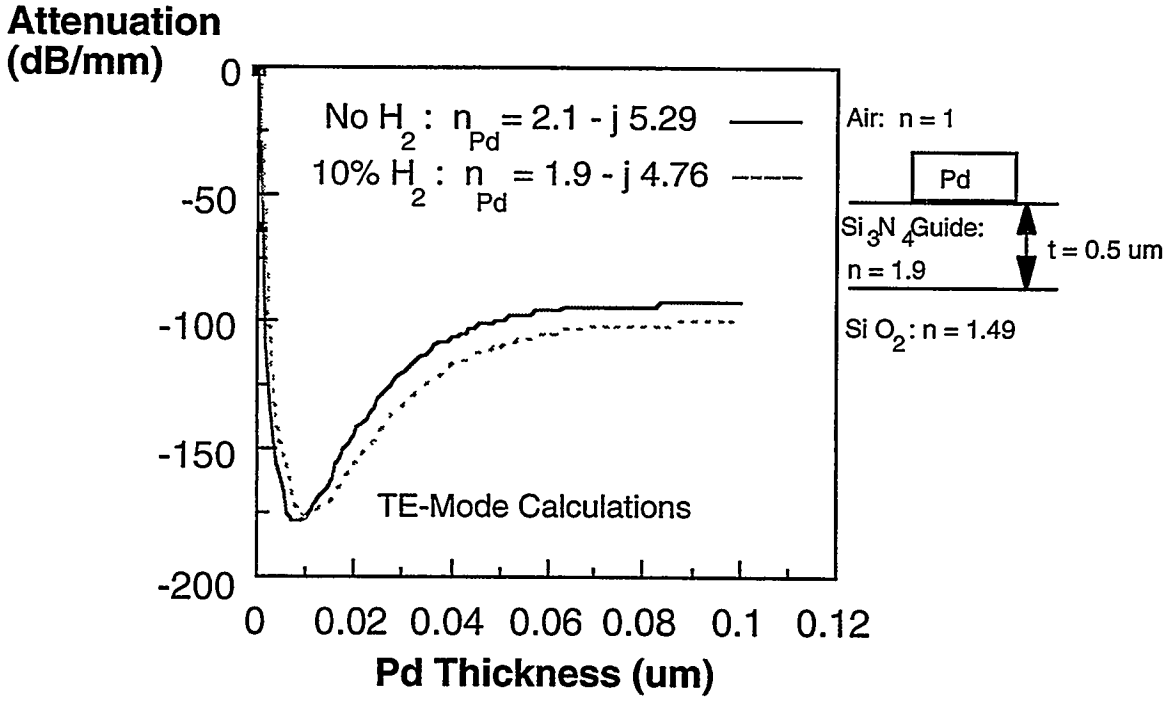


**Figure 10** Attenuation and hydrogen sensitivity of a Pd-clad $Si_3N_4$ waveguide.

## 3. THE DIODE JUNCTION STRUCTURE

The electrical cross-section of the basic GaAs/GaAlAs diode structure appears in Figure 11. These impurity doping levels yield a device that can operate as an LED, a photodiode, or as a photovoltaic cell. The structure represents a compromise between optimized doping for LED or detector performance. I-V curves were measured for devices fabricated from this structure. A sample curve appears in Figure 12. Note that the diode can be forward biased as an LED, reverse biased as a photocurrent detector, or zero-biased as a photovoltaic detector. Note also that the avalanche breakdown level is in excess of 27 V, so there is a large range of reverse bias levels that can be used in the photodiode mode of operation.

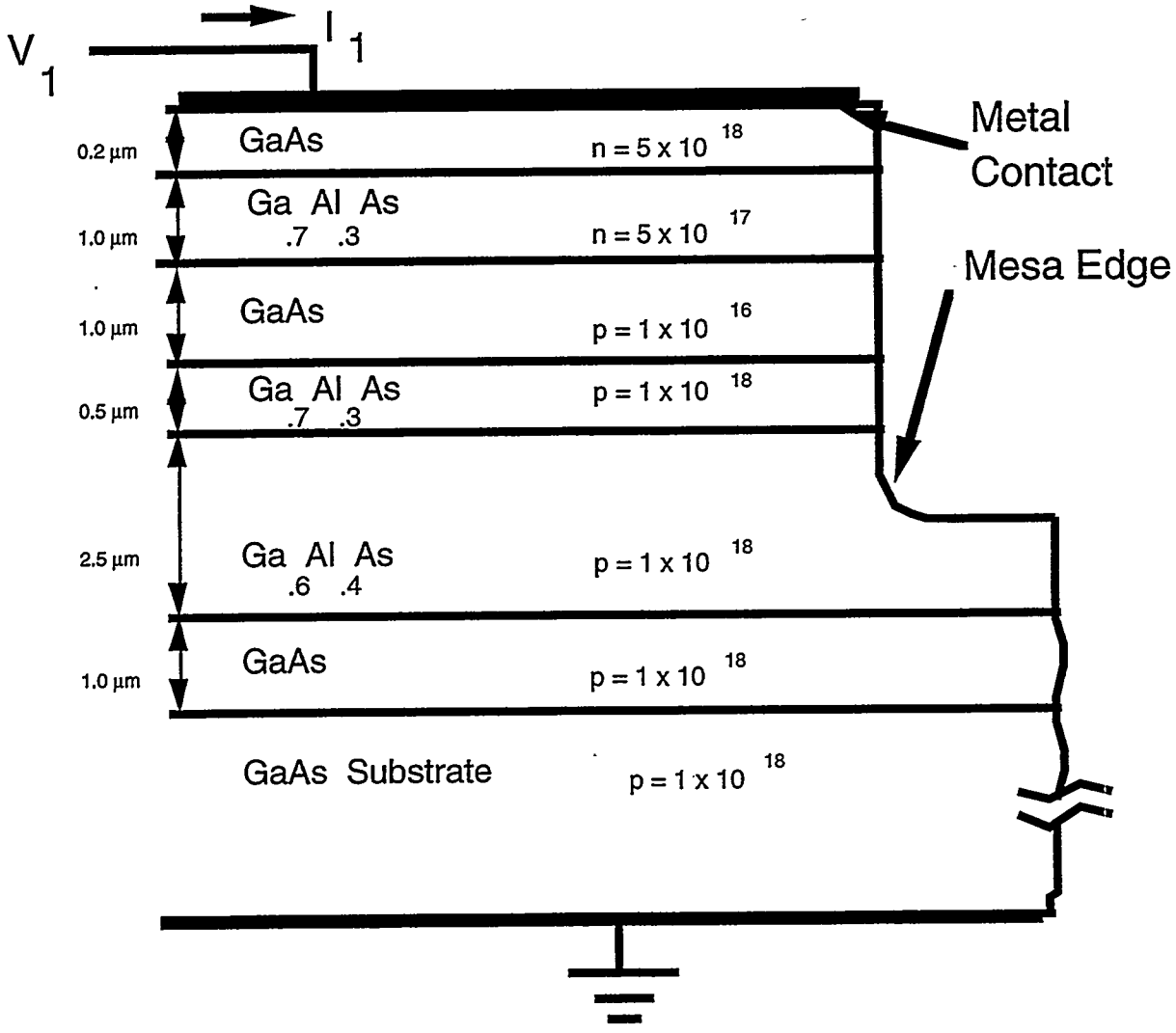


**Figure 11** Electrical cross-section of the heterojunction diode structure.

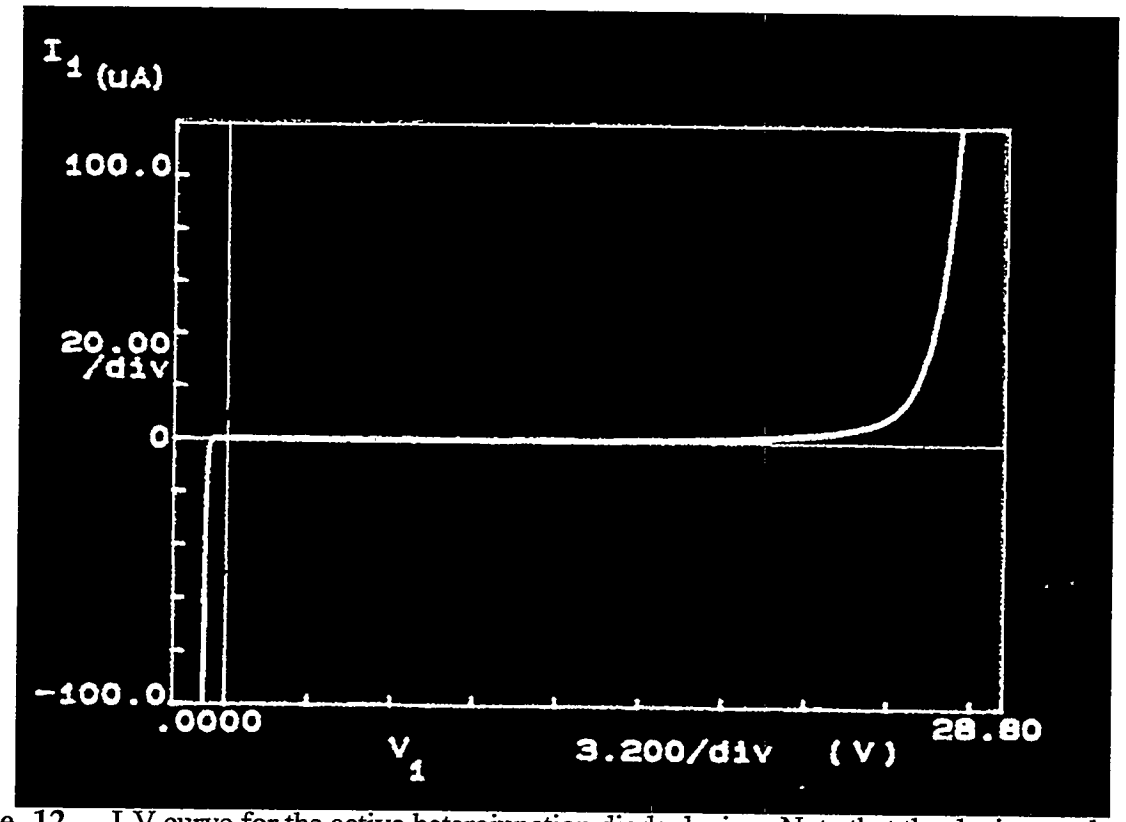


**Figure 12** I-V curve for the active heterojunction diode device. Note that the device can be forward-biased as an LED or reverse-biased as a detector.

## 3.1 LED Operating Wavelength and Output Profiles

The light output from the LED was measured by the use of an optical fiber probe, a fiber-coupled monochrometer, and a CCD television camera. The output wavelength under forward bias conditions was found to fall between 840 nm and 870 nm with its peak at 860 nm. This operating point corresponds to the expected band-edge of GaAs at room temperature.

The output light profile of the LED was measured and compared to calculated values. This near-field pattern was determined by viewing the output light emanating from the cleaved edge of a forward-biased device with a video microscope. The measured near field intensity profile is shown in Figure 13 along with the calculated profile for a zero order mode. Note that this pattern does not follow the quasi-Gaussian output profile calculated for the zeroth-order mode emanating from the guided-wave portion of the device (Figure 4). It could be a superposition of the several possible mode orders calculated for 860 nm as shown. The scale of the measured profile also indicates a large portion of the light emanating from the GaAlAs layers and the substrate. This is explained by the fact that light generated by spontanious emission in the semiconductor junction travels in all directions. Some of it will not be guided by the GaAs/GaAlAs heterostructure and can easily travel through the transparent GaAlAs layers to the GaAs substrate, as we see in the in the measured profile. Depending on the angle at which it encounters the substrate, it can travel up to 2.0 μm into the GaAs when it propagates normal to the epitaxial layers. Note that this matches published values of absorption coefficients for GaAs at 860 nm, where $\alpha = 1$ μm

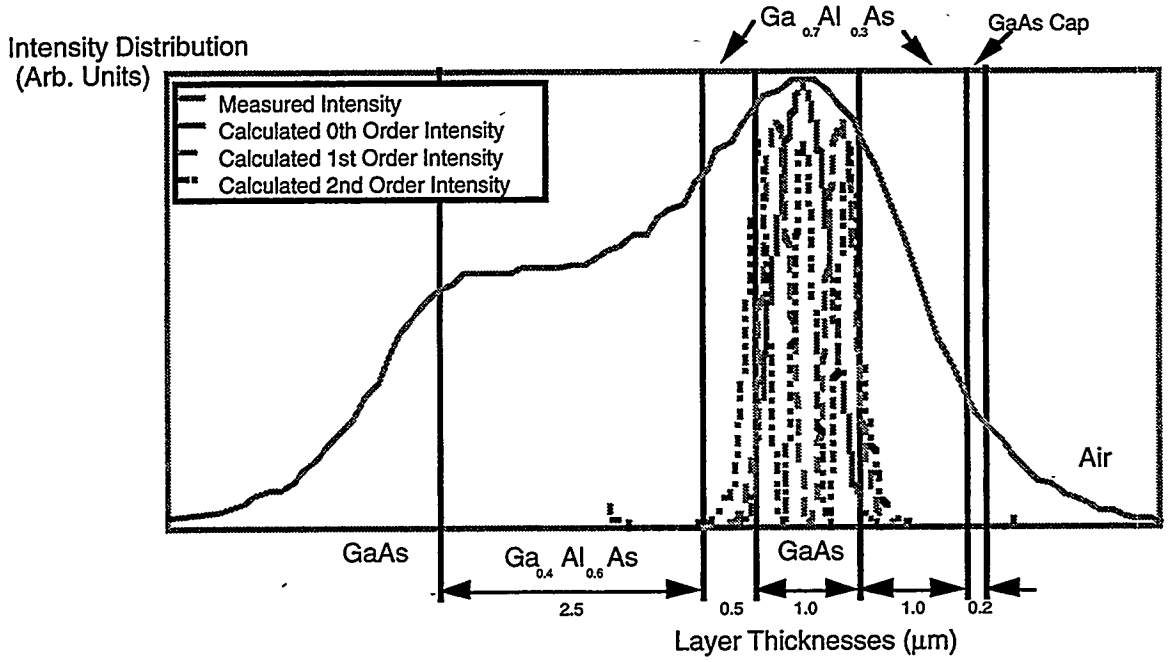


**Figure 13** Measured intensity pattern from the cleaved edge of the heterostructure LED, plotted with several possible guided-wave mode orders in the structure.

for $P(y) = P_o e^{-\alpha y}$. Here $P_o$ is the intensity at the GaAs-GaAlAs interface and y is the depth into the GaAs material [14].

In order to further compare these measured intensity patterns to calculated profiles, the guided-wave response of the diode structure was modeled at the measured center wavelength of 860 nm. The simulation showed the potential existence of not only the zeroth order mode, but a first order mode, and even a possible mode in the cap layer of the GaAs-GaAlAs structure as in Figure 14. Since the cap layer is relatively far from the emitting junction, its mode is not very likely to propagate. The first order mode is likely, however, and at least some of the light may appear in this mode as part of the intensity distribution in Figure 13. If a large amount of the light were in a first-order mode, it could cause problems for the coupling between the waveguide and the active device. This is illustrated by the combined structure of Figure 14. Here, the active device structure and waveguide are aligned as they would be in construction. Note that the zero-order fields line up well, indicating a good potential for zero-order coupling between the structures. The first-order modes, however, do not exhibit good coupling, as indicated by the fact they do not overlap well. It follows that this design depends on single-mode operation for efficient coupling. This represents a potential problem because the shape of the peak in the measured curve of Figure 13 and that of the calculated zeroth-order mode are much different from each other. The advantage of the broad LED mode, however, is that it may result in a reduced requirement for alignment tolerance between the LED and waveguide. The calculated and measured light profiles provide important results because they establish basic feasibility for coupling between the zero-order modes in the active diode and the dielectric waveguide, but indicate that the coupling will not be very efficient.

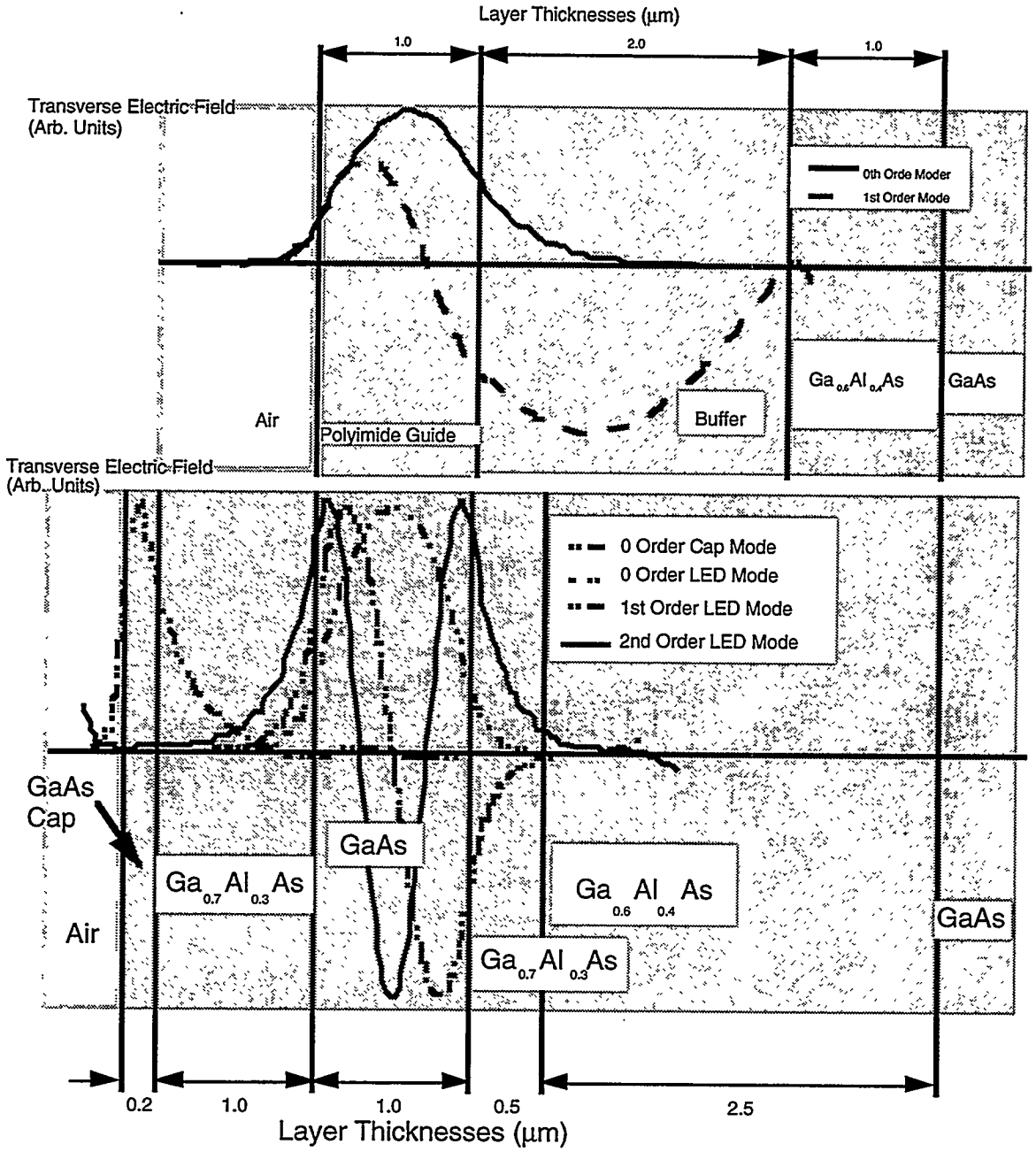


**Figure 14** Calculations of transverse fields for possible modes of the active diode and passive waveguide. Fields of the higher order modes do not match very well.

## 3.2 Photodetector Response

One of the most important potential design parameters associated with this device is the operational wavelength. As previously stated, the output wavelength from the LED will be near the band-edge of the GaAs material in the active device, and the design represents a compromise between LED and photodetector properties. It follows that the photodetector must respond to long enough wavelengths that

it will efficiently detect the light from the LED. Near the band-edge of the material the efficiency of this response can rapidly decrease, so the wavelength response becomes an important factor in device performance. In order to test the wavelength response of the diode structure, the cleaved edge of an active device was illuminated with a tunable Ti-Sapphire laser. The response in both biased and photovoltaic modes was then measured using a parameter analyzer. While the response was generally higher at shorter wavelengths, the signal at 860 nm was about 40 to 80 percent of the maximum above-band-edge response, depending on bias. Thus, basic operation of the sensor structure is assured, though efficiency is traded for simplicity in the active device structure.

## 3.3 GRINSCH Diode Structure

In order to improve the overall efficiency of our Tamper Sensors, the LDRD team decided to investigate alternative emitter and detector device designs. An extremely high-efficiency graded index separate confinement heterostructure (GRINSCH) single quantum well (SQW) laser design was being employed by another research team at Sandia and epitaxially grown material (from an outside supplier) was available for fabrication. The GRINSCH-SQW laser structure is shown in the table which follows:

**Table 1.** Graded-index separate confinement heterostructure (GRINSCH) diode junction structure.

| # | Layer | Material($Al_x$) | Type | Thick(μm) |
|---|---|---|---|---|
| 0 | Substrate | GaAs | n | 500 |
| 1 | Buffer | GaAs | n | 1.0 |
| 2 | Buffer | AlGaAs(0.15) | n | 0.5 |
| 3 | Confinement | AlGaAs(0.60) | n | 1.5 |
| 4 | Barrier | AlGaAs(0.60-0.30) | i | 0.2 |
| 5 | Well | GaAs | i | 0.01 |
| 6 | Barrier | AlGaAs(0.30-0.60) | i | 0.2 |
| 7 | Confinement | AlGaAs(0.60) | p | 1.1 |
| 8 | Contact | GaAs | p+ | 0.1 |

This structure had previously been used successfully in a forward and reverse biased mode as an integrated ring laser and detector [15]. It thus provides an excellent candidate for replacing the the heterjunction diode of Figure 11. It would have major advantages in coupling efficiency over the LED-based structure, at most of its light would be guided, and could be expected to easily couple into the dielectric waveguide of Figure 4. This was verified by calculations of the expected field profile of a GRINSCH laser output in its fundamental transverse mode, which showed a field width of about 1 μm (an excellent match to the fundamental mode of the dielectric guide of Figure 4). Such a profile should also be approximated by a GRINSCH LED, though coupling to the fundamental mode would be less efficient, as was shown for the heterojunction LED of Figure 13.

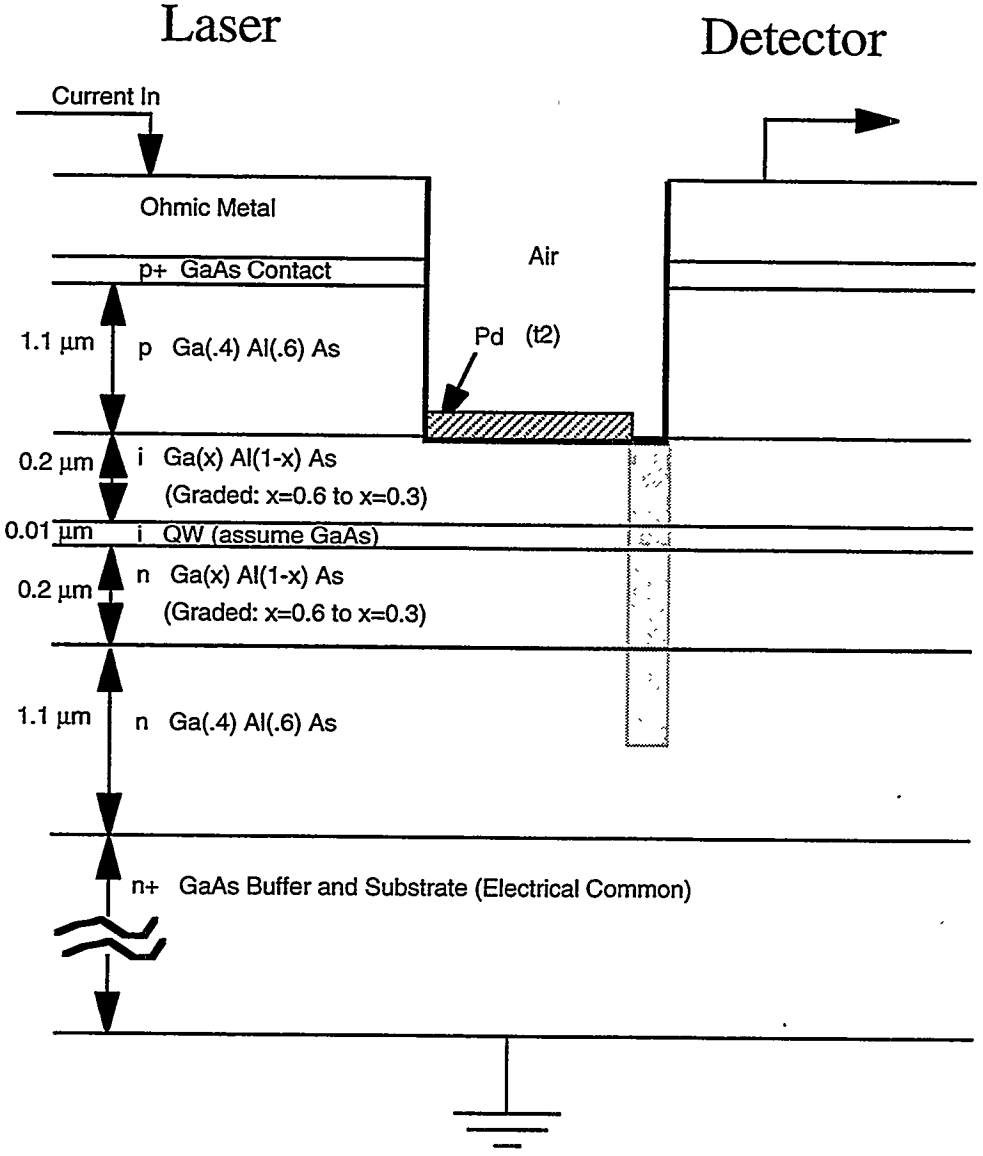


**Figure 15** Monolithic hydrogen sensor made from a GRINSCH laser structure.

Additional calculations of the GRINSH laser structure showed that it could act as a monolithically-integrated hydrogen sensor as shown in Figure 15. Here, the laser and detector would be separated by a short length of implanted and etchedmaterial . A palladium layer would then be applied. If the buffer layers are etched to a depth where there is sufficient evanescent field overlap with the quantum well guide, then the interaction with the palladium can be strong enough to cause an index-dependent attenuation. The expected attenuation would be very dependent on the accuracy of the etch, and the overall attenuation (and resulting sensitivity to hydrogen) would rise as the palladium is placed closer to the quantum well guiding layer. The calculated TE attenuation curve for the case where the Pd layer is against the graded buffer appears in Figure 16. Note here that, although the overall attenuation is large, a measurable difference (up to 5 dB) between the attenuation in the presence and abscence of hydrogen can occur for thin Pd layers. Because of the high output power from a structure such as a GRINSCH ring laser, this large attenuation could be accomodated. An important conderation, however , is the fact

that the etched sensor section of the structure in Figure 15 would need to be electrically pumped to maintain transparency to the laser light in that region of light propagation.

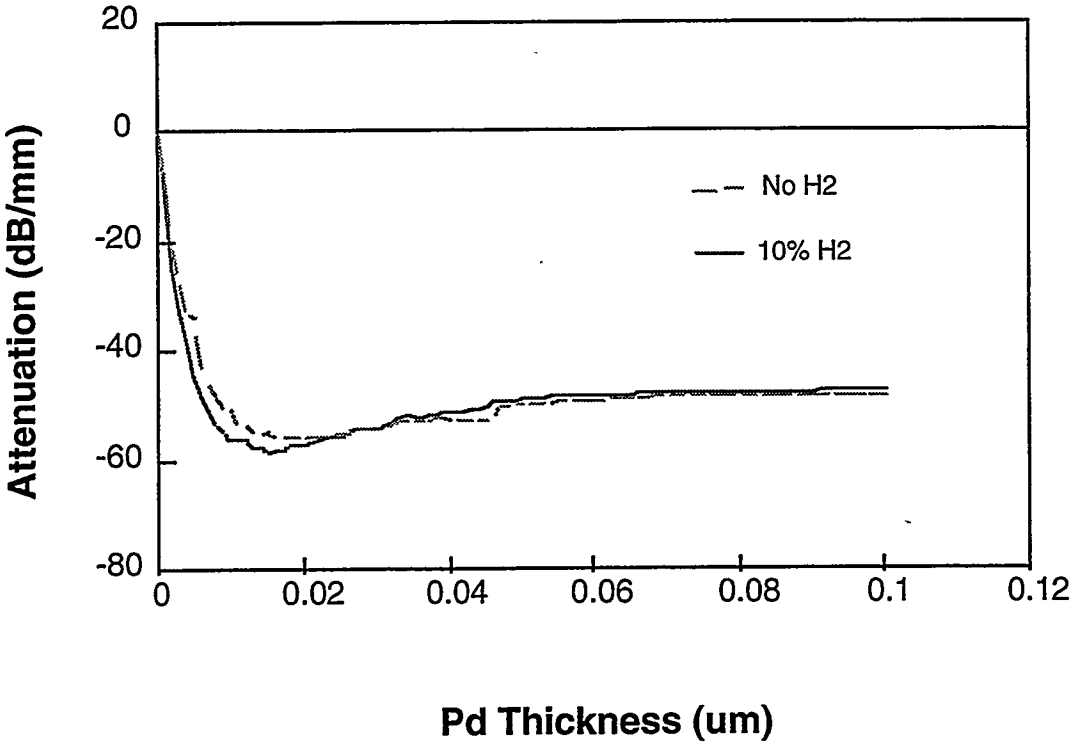


**Figure 16** Attenuation of the monolithic GRINSCH structure in the presence and abscence of hydrogen when the palladium layer is placed at the graded layer as in Figure 15.

# 4. MEASURED WAVEGUIDE PROPERTIES

The basic properties of polyimide waveguides are well established.[3] The materials and structure used here have been verified by measurement of waveguide loss for a planar polymer guide structure such as that of Figure 4. The loss in the guide was measured by launching light into one of two propagating modes via a prism coupler. The scattered light from the guide was measured by video imaging. The intensity drop was plotted as a function of distance along the guide. An exponential fit to those plots revealed a loss of 1 dB/cm for the $TE_0$ mode and 9 dB/cm for the $TE_1$ mode. This is expected, since the $TE_1$ mode interacts more strongly with the absorptive substrate as in the field plot of Figure 6. The above loss values were obtained for waveguides that had only been "soft-baked" at 180°C for 90 seconds to cure the polyimide. An additional bake time of 60 minutes at 250 °C was also used to harden and stabilize some of the waveguides. These "hard-baked" waveguides exhibited measured losses that were a factor of 2 to 3 greater than those of the standard polyimide guides.

Waveguide and buffer refractive index was verified by two different measurement methods. Using both ellipsometry and prism coupling, the refractive index of the polyimide waveguide was measured at 1.67. Index for the $SiO_2$ buffer was found to be 1.49. This indicates that the $SiO_2$ deposition is slightly silicon-rich and the polyimide guide is operating as expected. These results were used to iterate modeling efforts and provide a more accurate prediction of guide performance.

# 5. FABRICATION ISSUES AND TRANSFER FUNCTION MEASUREMENTS

The fabrication steps for the tamper sensor involve patterning, deposition, and annealing of ohmic contact metal on the top and bottom of the wafer, patterning and etch of the mesa structure. Next is deposition and patterning of the buffer layer. The final steps are spinning, patterning, and curing of the polyimide layer. Various changes in the fabrication process were implemented to improve the overall efficiency of the sensor structures.

## 5.1 Basic Fabrication Steps

The basic processes that will influence tamper sensor performance, (i.e. photodetector response for a given LED current input) are the etch, deposition of buffer, and spinning and curing of the polyimide waveguide. The etch and deposition processes must be well controlled so the LED and waveguide will properly line up as in Figure 6. The most severe problem encountered with fabrication of tamper sensor devices was the ability to obtain devices with the ideal mesa-edge sidewalls of Figure 4. Many wet-etch methods result in sloped sidewalls. This would greatly reduce the efficiency of coupling, since the light encounters an angled interface with a large refractive index difference as it exits the LED. Such a profile puts much of the light beyond the critical angle for reflection. Initial devices were fabricated by wet etch techniques with sloped sidewalls. They exhibited poor coupling between the LED and photodetector. Other wet-etch methods have shown improvements in the sidewall slope and were used to fabricate tamper sensor devices as in Figure 4. The most nearly vertical sidewalls are obtained with Reactive Ion Etching (RIE) or Reactive Ion Beam Etching (RIBE). Thus, these are the preferred methods for active device etching and have been incorporated into the processing sequence.

## 5.2 Improvements in Fabrication

One of the main goals of the second year of this LDRD was to improve the overall operating efficiency of the tamper sensors. During the second year, five wafers were processed with numerous variations in the individual processing steps. As discussed previously, vertical mesa edge sidewalls is critical to coupling between the waveguide and emitter and detector elements. Consequently, during the second year all wafers were processed using the RIBE patterning process. Nearly all of the changes made in the basic process, which was briefly outlined in the previous section, resulted in marked improvements in device efficiency. Since the number of changes made and variations investigated is so numerous, each wafer is discussed separately in the following paragraphs.

The first wafer was processed to establish a consistent baseline efficiency using the process flow outlined in section 5.1. Briefly, the baseline process wafer, "Sandia 13-C", which contained the standard Tamper Sensor layer structure shown in Figure 4, was processed with the normal mask set, normal Brewer Scientific T-15010 polyimide, and SiO2 patterning such that SiO2 is removed from the sidewalls of the mesa. After these devices were tested, measured efficiencies were found to be comparable to previously fabricated devices ($I_{photocurrent}/I_{emitter}$ = 5 x $10^{-6}$ to 2 x $10^{-7}$ as wveguide length was varied from 0.5 cm to 2.0 cm) [16]. Based on these results, the LDRD team identified several areas for potential improvement in performance.

The second wafer processed, "Sandia 13-D", was grown using the standard layer structure, but was processed using a new mask set and a new polyimide. Among other things, the new mask set had an improved emitter metal design such that the emitter metal would only contact a fraction (~1/3) of the top of the emitter mesa, directly next to the waveguide. We anticipated that this would result in an immediate ~3-fold improvement in efficiciency since current would preferentially channel through the mesa edge closest to the waveguide. As was discussed earlier in section 4, a new photo-defineable polyimide, OCG

Probimide 408, was characterized in a slab waveguide fashion and found to have much lower loss characteristics than the Brewer polyimide. Additionally, since it is directly photodefineable, a simpler ~1.1 μm thick process for patterning the polyimide waveguide was developed. The OCG polyimide acts like a negative resist in that whatever is exposed to sufficient UV light remains after develop. Thus, after a new negative tone waveguide mask was received, processing of wafer "Sandia 13-D" was completed. As expected, these devices were much more efficient than the baseline devices. Here, output current ratios of $I_{photocurrent}/I_{emitter} = 5 \times 10^{-6}$ to $2 \times 10^{-7}$ were measured as waveguide length was varied from 0.5 cm to 2.0 cm [16].

The third wafer processed, "Hohimer TS-1", was grown using the GRINSCH highly efficient emitter laser structure described in Section 3.3. This structure was processed in the same fashion as the second wafer (new mask set, new polyimide) but, based on SEM photos of completed devices from the second wafer, the SiO2 buffer patterning process was changed. The SEM photos revealed that due to alignment error and the inherent non-uniformities in wet chemical etching of the SiO2, light was not coupling ideally into the polyimide waveguide. Consequently, the masks used for the mesa etch and SiO2 patterning steps were changed so that the $SiO_2$ buffer would remain on the sidewalls of the mesa after patterning. Additonally, after RIBE patterning, a SEM characterization step was added to determine more precisely the exact thickness of buffer layer required for proper coupling. Finally, since the GRINSCH structure has a highly conductive cap layer on it which would cause severe current spreading effects, this layer was selectively removed after the ohmic metal patterning step. The GRINSCH-based tamper sensors processed in the above fashion were approximately an order of magnitude more efficient than previously fabricated devices (output-to-input current ratios of $5 \times 10^{-4}$ to $6 \times 10^{5}$) [16].

After measuring the much higher efficiency, fabrication of another GRINSCH-based wafer, "Hohimer TS-2", was initiated with some rather radical processing changes. The LDRD team was looking for ways to improve the coupling efficiency into and out of the waveguide and the concept of using the GaAs/AlGaAs structure itself as a waveguide was proposed. This would totally eliminate any losses due to waveguide-to-device coupling and it also greatly simplified the processing sequence. We were able to fabricate this fourth wafer using only five process steps (p-ohmic pattern, p+ layer etch, combined mesa and waveguide pattern, n-ohmic deposition, anneal). The only complicated step was figuring out a way to pattern the mesa and waveguide at the same time. This was performed successfully by using image reversal photolithography with a double align - double expose process. Another change which was incorporated to optimize the emitter's efficiency was using a new (third version) emitter mask. On this mask 10 combinations of the dimensions of the emitter metal were varied in length. Here the goal was to optimize the contact geometry by minimizing the amplification threshold. Unfortunately, after testing the devices, we realized that current was leaking from the emitter to the detector through the III-V waveguide. Consequently, the wafer was patterned with a thick resist in such a way that only a small ~50 μm region of the waveguide near the emitter was unprotected. The wafer was then subjected to a, proton ($H^+$) isolation implant (as indicated in Figure 15) to remove this leakage path. This did successfully eliminate our leakage problem.

As was stated in section 3.4, another layer design was created which was based on the standard structure shown in Figure 4. In this structure, the goal was to improve the efficiency by displacing the p-n junction away from the heterojunction and remove this barrier, or "spike", which hinders current flow. The structure was subsequently grown in the CSRL by OMVPE. This fifth and final wafer, "Xd0910C", was processed in the following fashion. We used the new mask set (including the variable emitter metal mask), new OCG polyimide, RIBE, SEM'd the structure after RIBE for SiO2 thickness determination, left SiO2 on the mesa sidewalls, and performed the selective n-contact layer removal etch after n-ohmic patterning.

As indicated previously, one of the goals of the LDRD was the demonstration of chemical sensing. This was successfully performed for the test case of detecting 4% H2 in N2, as will be described. To achieve

this a mask was designed with varying (0.1 to 1.0 mm) lengths, full waveguide width features to allow for loading of a small fraction of the waveguide with Pd. Parts of wafers "Hohimer TS-1" and "Sandia 13-D" were re-patterned with this mask using a thick liftoff resist and ~700 Å of Pd was deposited and patterned onto the polyimide waveguide via liftoff. These devices were packaged and subsequently tested as $H_2$ sensors.

## 5.3 Initial Transfer Function Measurements: Photovoltaic Response Mode

The design parameters and test results described above were applied to the fabrication of an initial test set of tamper sensor devices. These first devices use 100 μm x 200 μm active LEDs and photodetectors defined by a RIBE etch, well optimized for vertical sidewalls. Each LED-photodetector device pair is connected by a 50 or 100 μm wide polyimide waveguide up to 1.5 cm long. Thus, the waveguides are vertical slab-type guides with geometric guiding in the horizontal direction. The transfer function for two devices connected by a 100 μm guide of length 0.5 cm is shown in Figure 17. Because these devices were RIBE etched, they had the most vertical sidewalls, and hence the most efficient coupling that could be expected for a given LED-photodetector pair. The smooth sidewalls that result form RIBE also tend to reduce surface recombination, which makes the LED and detector both more efficient. In the transfer function of Figure 17, a current was applied to the LED as shown on the x axis of the graph. The resulting forward voltage on the LED is plotted along the left y axis and the photovoltaic response from the photodetector is displayed on the right axis. Note that 450 mV is obtained from the detector with 100 mA applied to the LED.

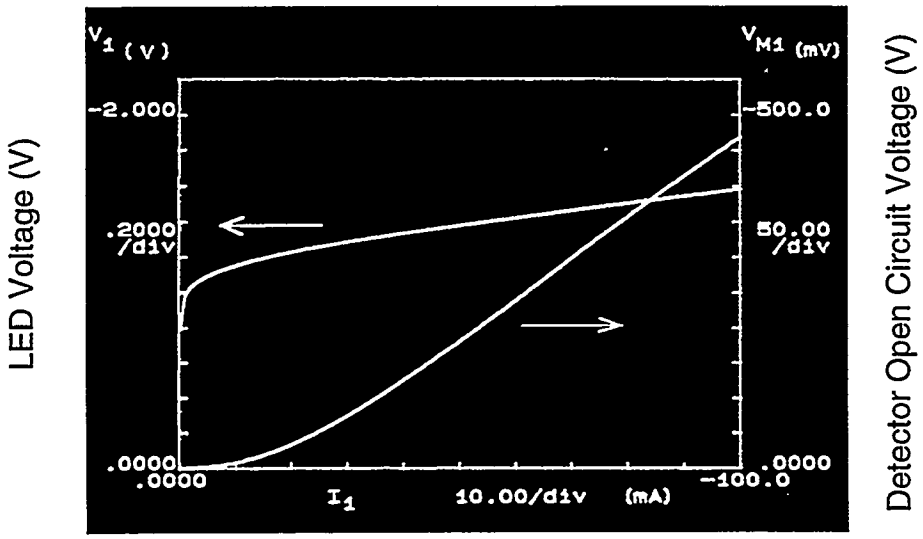


**Figure 17** Transfer function of the LED-Waveguide-Detector of Figure 1 when detector is operated as a photovoltaic device.

The transfer function response of the sensor could be greatly improved by channeling current to the edge of the LED. In the design, most of the generated light is wasted, since it is generated far from the mesa edge, it is re-absorbed by the GaAs active layer before it can reach the waveguide. Thus, the design is very inefficient, though it worked for proof-of-concept studies. Note also that this effect makes the smooth RIBE etch especially important, since the light must be generated near the LED mesa edge to be coupled into the waveguide.

Another important aspect of the transfer function test is that the voltage monitor used to measure the photodetector output hasda 1.0 MΩ input impedance. For the low input powers of the wet-etched devices, output voltage levels went from 50 mV at 100 mA to 0.4 V when the load impedance was changed from 1.0 MΩ to 10 MΩ. This was due to the fact that for small input powers, the generated photocurrent was split between the 1.0 MΩ external load and the internal leakage current, thus reducing the terminal voltage. There was a much smaller increase in signal for the RIBE-etched device of Figure 7 when load impedance was changed. For this case, the photocurrent was already much larger than the internal leakage current. In actual practice, the use of appropriate output buffer amplifiers will produce the desired high output impedance. In order to keep the results consistent, the output signals into 1.0 MΩ continued to be used for test purposes.

In current mode, the short circuit photocurrent was measured for various diodes to give the efficiency data quoted above for detector curent as a function of input LED current.

## 5.4 Absorber Interaction Measurements and Calculations

Fabricated devices were tested for absorber interaction by the application of ground silicon "dust". Silicon was chosen because it is highly absorptive at the wavelength of interest and has a refractive index that is much higher than that of the polyimide waveguide.[6] In initial experiments, the dust was applied directly to the guide by sprinkling. Interactions with the waveguide were too weak to be measured due to the odd shapes of the pieces of dust. On a microscopic scale, the silicon would not lay flat on the waveguide, so there was always a layer of air between most of the silicon and the polyimide. This is similar to the case of the waveguide field profile in Figure 4 where air is the cover layer. Here, very little of the evanescent tail in the field of the guided wave extends into the air layer. Thus, there is little or no interaction across the air gap formed between the guide and the silicon dust. Pressure was applied to increase the interaction of the silicon dust by decreasing the air gap. In this case however, silicon tended to embed in the waveguide and cause a permanent attenuation of the signal. This is not desirable, since the tamper sensing function depends on *reversible* interactions between the waveguide and absorber as in Figure 1.

The difficulties with waveguide-absorber interaction were addressed by suspending the absorbers in material having a refractive index closer to that of the polyimide waveguide. This would draw the evanescent field out from the surface of the waveguide and increase the interaction length of the field with the absorbers. Several index matching fluids were tried, having refractive index values between 1.4 and 1.5. In one experiment, a glycerol mixture was used as an index matching fluid having refractive index 1.46. Absorber interaction results were measured as in Figure 18. When first applied to the surface of the waveguide, the index matching fluid did not change the response curve from the baseline shown in step 1 of Figure 18. A silicon absorber, however, reduced the response from the step 1 curve of Fig. 18 (48 mV at a 100 mA input) to the step 2 curve (24 mV at 100 mA). The absorber was then mechanically removed from the waveguide surface. Some debris from the silicon remained suspended in the matching fluid however, and interacted even more strongly with the waveguide as in the

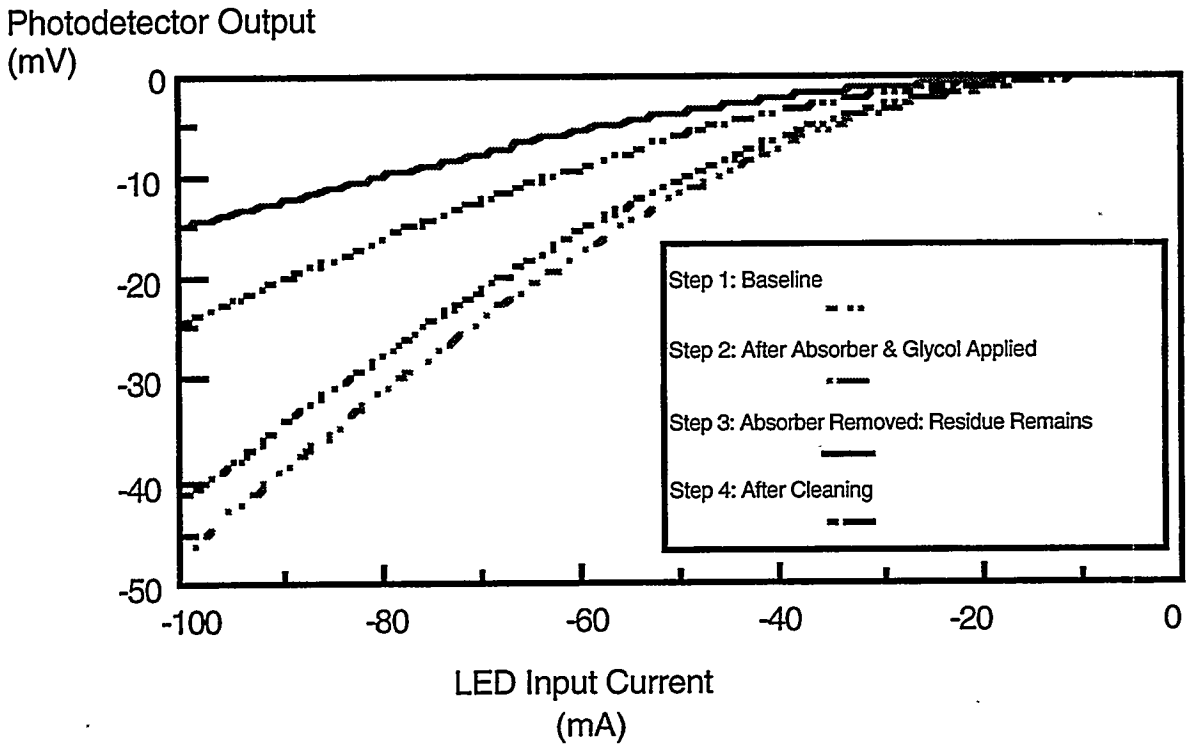


**Figure 18** Tamper sensor transfer function with and without absorber interaction.

step 3 curve of Figure 18 (15 mV at 100 mA). When the glycerol was washed off the waveguide with methanol, the response returned to a level close to the original baseline (step 4 in Figure 18).

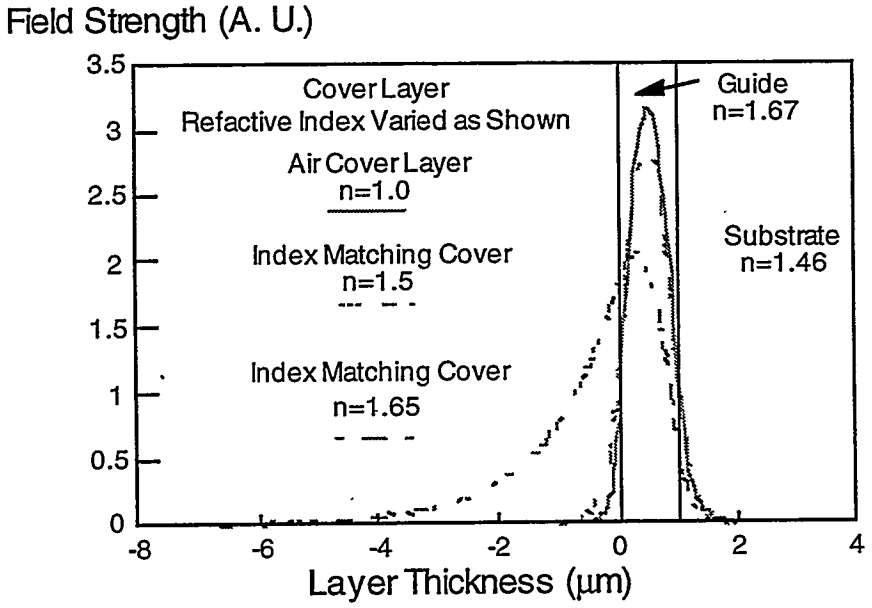


**Figure 19** Field plots showing evanescent field tail as a function of over-layer refractive index.

In an actual tamper sensing application, the index matching fluid would be replaced by an optical epoxy having an appropriate refractive index. It would serve both as a matching and adhesive medium The higher the index, the better, since the evanescent field tail would be drawn further from the waveguide surface. This is illustrated by the guided-wave field distribution calculations of Figure 19. Here, the refractive index of the semi-infinite cap layer of a three-layer waveguide is varied. Note for air that the evanescent field extends only several tenths of a micron out of the waveguide. For a cover layer with refractive index 1.5, the evanescent field tail still extends less than a micron out of the surface. For a cover layer with refractive index 1.65 however, the evanescent field extends over 5 microns from the surface of the waveguide. Thus, any absorbers that were within a few microns of the guide would interact strongly to attenuate the guided wave.

# 6. HYDROGEN SENSOR MEASUREMENTS

Over the years a number of hydrogen sensors have been reported that utilize the interaction between hydrogen and palladium metal [17]. Formation of palladium hydride produces changes in several physical properties including conductivity and index of refraction. These changes can be used as the basis for hydrogen sensing. In the sensor reported here and described in the calculations of Section 2, palladium is coated onto a dielectric waveguide and changes in the optical properties upon hydride formation result in a change in the amount of light transmitted through the guide. This is in contrast to a similar, previously described sensor [13] in which the hydriding of the palladium film alters the phase of the light propagating through the waveguide.

This sensor utilizes an integrated GaAs device containing an LED and a photodiode connected by a dielectric waveguide on a single chip [18] as described in Section 1. The device structure consists of GaAs and AlGaAs epitaxial diode layers grown on a GaAs substrate by LP-MOVPE as in Figure 11. The devices are fabricated using standard optical contact lithography for patterning and E-beam evaporation/RTA for ohmic contact formation. Reactive ion beam etching (RIBE) is required for mesa isolation since vertical side walls improve coupling efficiency in and out of the waveguide. A thick (2.0 μm), low stress, $SiO_2/Si_3N_4$ PECVD dielectric deposition process was developed to minimize evanescent coupling of the waveguide light into the GaAs substrate. A low loss (1-2 db/cm), photodefinable polyimide (OCG, Probimide 408) was used to form the 250 to 500 μm wide by 3 to 10 mm long by 1 μm thick optical waveguide, and this was found to greatly improve the light transmission and detection. After polyimide curing, varying lengths (0.1 - 10 mm) of 70 nm thick palladium films were evaporated onto the waveguide and patterned by liftoff. The completed devices were packaged in 14 pin DIP packages and tested.

Testing was performed using a computer controlled gas flow system in which the hydrogen concentration can be varied over a wide range. The hydrogen sensing test was started by first turning on

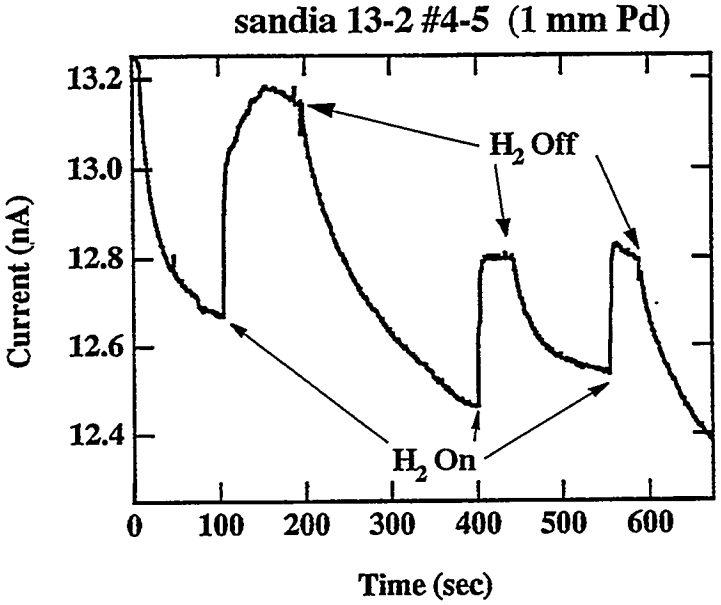


**Figure 20** Hydrogen sensor response (from air to 3.5 % $H_2$ in $N_2$).

a gas f;low of 100sccm pure $N_2$ and passing a constant current of 50 ma through the LED and monitoring the short circuit current out of the photodetector. Once a stable baseline was established, the sensors were exposed to alternating flows of 100 sccm of 3.5% $H_2$ in $N_2$ and pure $N_2$. A typical response curve is shown in Figure 20. As shown, the response time is reasonable and for this 1 mm long Pd stripe , the magnitude of the detected signal is about 4%. As expected from the calculations the presence of hydrogen results in a decrease in photocurrent or an increase in the attenuation of the light propagating through the polyimide waveguide.

The sensitivity of the device to hydrogen depends on the coupling between the propagating light and the palladium film via the evanescent field. This was calculated as in Section 2.2. The model predicts a sensitivity to hydrogen which increases with the length of the palladium stripe along the 1 micron thick waveguide and is independent of the palladium film thickness above 20 nm. Results for palladium stripe lengths up to 1.0 mm are shown in Figure 21.

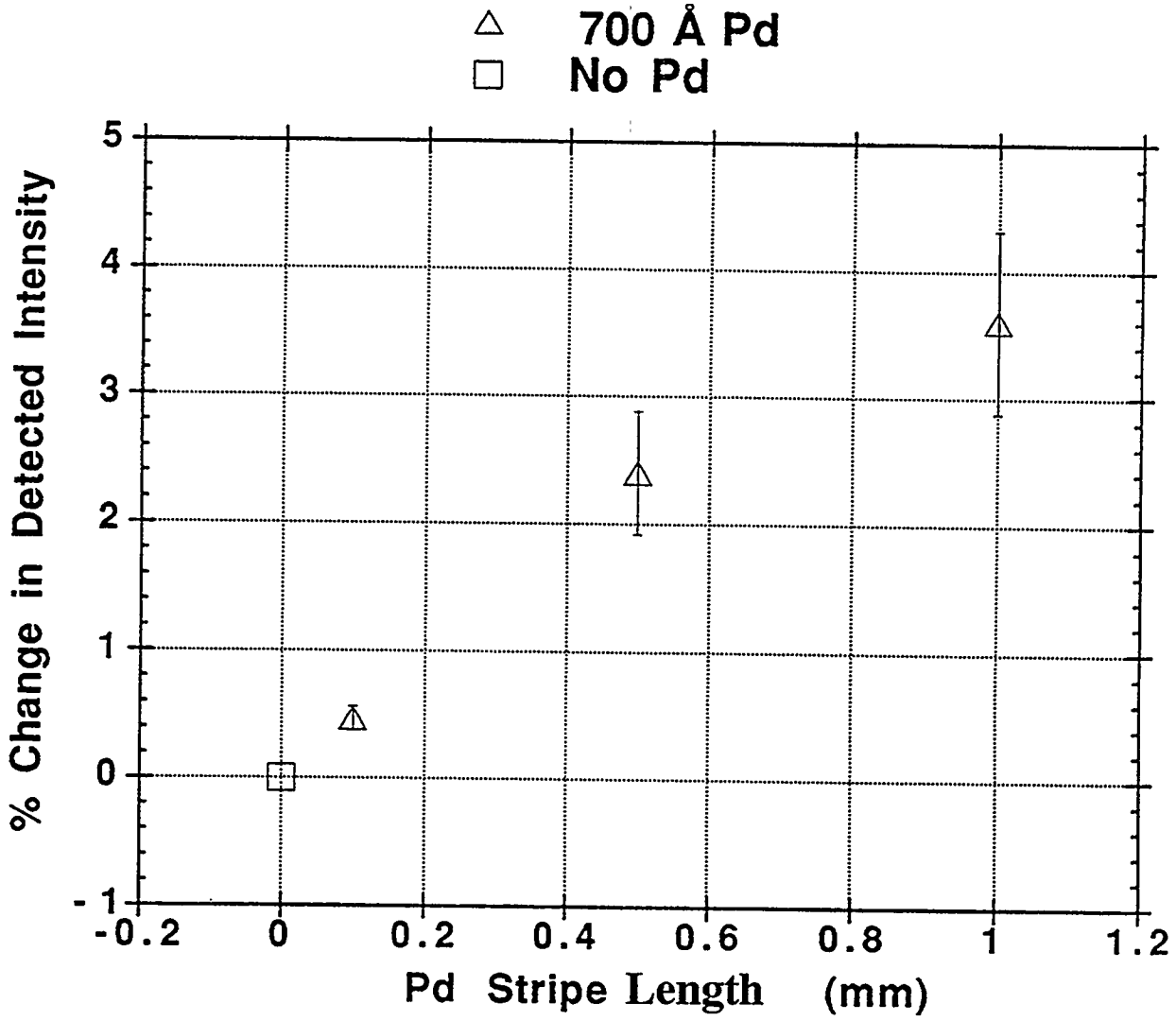


**Figure 21** Hydrogen sensor response for various lengths of Pd on the dielectric waveguide.

# 7. CONCLUSION

In this work we have shown an integrated optical sensor arrangement that combines active LED and detector devices with a dielectric waveguide. We discussed the properties of this integrated device and improved signal levels by the use of modeling, advanced fabrication techniques such as RIBE, and advanced structures such as GRINSCH diodes. Our experiments with absorber interaction have shown the basic feasibility of using the device as an in-situ tamper sensor for integrated circuit packages when the absorber is suspended in an index matching medium.

Finally, we have indicated how this device can be used for other functions such as chemical sensing with a basic demonstration of hydrogen sensing using a Pd cladding on the dielectric waveguide structure. While the devices described have many of the limitations and advantages exhibited by other hydrogen sensing devices based on palladium hydride formation, they are monolithic integrated devices on a GaAs chip. This has two distinct advantages: first since they are made using conventional IC fabrication processes, they are more amenable to low cost mass production than hybrid sensors, and second, since GaAs is more radiation hard than silicon, our GaAs-based sensor may offer distinct advantages over integrated silicon devices in high radiation environments that might be encountered in cleanup and remediation activities in the DOE complex. In addition, the integrated functionality offered by these chips could allow insertion into other electronic modules or chip packages for in-situ monitoring techniques that could extend the usable life of electronics in nuclear stockpile and other applications.

Future work could concentrate on sensor arrays or integrated strucutures, and could make use of increasing levels of integration with other technologies such as micromachines to realize smart, multi-funtion sensors in small packages.

# 8. REFERENCES


1. T. Tamir, ed. *Topics in Applied Physics*, vol. 7, *Integrated Optics*,2nd ed., New York, Springer-Verlag (1979).

2. R. G. Hunsperger, *Springer Series in Optical Sciences*,vol. 33, *Integrated Optics: Theory and Technology*, New York: Springer-Verlag (1982).

3. C. T. Sullivan, B. L. Booth, A Husain, "Polymeric Waveguides", *IEEE Circuits and Devices*, vol. 8, No. 1, pp. 27-31, January, 1992.

4. K. Furuya, B.I. Miller, L.A. Coldren, and R.E. Howard, "A Novel Deposit/Spin Waveguide Interconnection (DWSI) for Semiconductor Integrated Optics", *IEEE J. of Quantum Electronics*, Vol. QE-18, No. 10, pp.1783-1789, October, 1982.

5. H.E. Jackson, D.E.Zelmon, J.T. Boyd, and P.B. Kosel, "Fabrication of Graded Index Planar Optical Waveguides on Silicon Exhibiting Low Scattering", *Proc. of the SPIE*, Vol. 408, pp.34-37, 1983.

6. R.F. Carson and T.E. Batchman, "Multimode Phenomena in Semiconductor-Clad Dielectric Optical Waveguide Structures", *Applied Optics*, Vol. 29, No.18, pp.2769-1780, June, 1990.

7. K. Sasaki, Y. Kudo, H. Watanabe, and O. Hamano, "Determining the Optical Constants of Vacuum Evaporated II-VI Compound Thin Films with Optical Waveguides", *Applied Optics*, Vol. 20, No. 21, pp. 3715-3718, November, 1981.

8. D. R. Larson and D.L. Veasey, "Localized Plasma Etching for Device Optimization", *J. of Vacuum Science and Technology B*, Vol. 10, No. 1, pp.27-29, January, 1992.

9. G. Stewart, B. Culshaw, D.F. Clark, and I. Andonovic, "Improvement in the Performance of Evanescent Wave Chemical Sensors by Special Waveguide Structures", *Proc. of the SPIE*, Vol. 1386, pp. 230-238, 1990.

10. R. B. Smith and G. L. Mitchell, "Calculation of Complex Propagating Modes in Arbitrary Plane-Layered, Complex Dielectric Structures", Technical Report 206, U. Washington Department of Electrical Engineering, National Technical Information Service Report PB-177, Seattle, WA 1977.

11. M. A. Butler, "Micromirror Optical Fiber Hydrogen Sensor", *Sensors and Actuators*, Vol. B22, pp. 155-163, (1994).

12. Y. Yamamoto, T. Kamiya, and H. Yanai, "Characteristics of Optical Guided Modes in Multilayer Metal-Clad Planar Optical Guide with Low-Index Dielectric Buffer Layer," *IEEE J. of Quantum Electronics*, Vol. QE-11, No. 9 pp.729-736, September, 1975.

13. A. Bearzotti, C. Caliendo, E. Verona, and A. D'Amico, "Integrated Optic Sensor for the Detection of $H_2$ Concentrations", *Sensors and Actuators*, Vol. B7, pp. 685-688, (1992).

14. S. Sze, *Semiconductor Physics, 2nd. ed.*, New York: John Wiley & Sons, Smith p.750 (1981).

15. J. P. Hohimer, G. R. Hadley, G. A. Vawter, and D. C. Craft, *Semiçonductor Ring Lasers*, SAND92-2760, Sandia National Laboratories, Albuquerque, NM, March, 1993.

16. M. L. Lovejoy, Internal Memorandum, August 30, 1993.

17. A. Mandelis and C. Christofides, Sensors and Actuators B 2, p. 79, (1990).

18. R. F. Carson, S. A. Casalnuovo, and M. B. Sinclair, Proc. SPIE 1791, p. 140, (1992).

DISTRIBUTION:

| | | |
|---|---|---|
| 1 | MS 1425 | M. W. Scott, 1307 |
| 1 | MS 0603 | A. Owyoung, 1312 |
| 1 | MS 0603 | T. E. Zipperian, 1313 |
| 2 | MS 0603 | S. A. Casalnuovo, 1313 |
| 1 | MS 0603 | C. T. Sullivan, 1313 |
| 1 | MS 1425 | S. J. Martin, 1315 |
| 5 | MS 1425 | M. A. Butler, 1315 |
| 1 | MS 1082 | D. W. Palmer, 1333 |
| 10 | MS 0874 | R. F. Carson, 1342 |
| 2 | MS 1405 | M. B. Sinclair, 1812 |
| 1 | MS 0529 | M. L. Lovejoy, 2346 |
| 1 | MS 0877 | J. P. Anthes, 5903 |
| 1 | MS 0161 | J. P. Hohimer, 11500 |
| 1 | MS 1436 | LDRD Office, 1011 |
| 1 | MS 9018 | Central Tech Files, 8940-2 |
| 5 | MS 0889 | Tech Library, 4414 |
| 2 | MS 0619 | Review and Approval Desk, 12690<br>For DOE/OSTI |
| 3 | MS 0161 | Patent and Licensing Office, 11500 |